Enhancing Wear Resistance and Microstructural Evolution of Brass Through Laser Shock Peening

Yaowen Chen[1] · Yuanyuan Sheng[1] · Ying Wang[1] · Min Ji[1] · Haijun Pan[1] · Feichi Zhang[2] · Lin Liu[1]

Abstract

In this work, the effect of laser shock peening (LSP) on the microstructure evolution and deformation mechanism of a lubricated brass surface layer has been systematically investigated. Prior to LSP treatment, fatigue and adhesive wear were identified as the primary wear mechanisms of the brass surface layer. However, after LSP treatment, abrasive wear became the dominant wear mechanism. The deformation mechanism of the untreated brass layer was primarily governed by disloca-tion slip, leading to poor tribological performance. LSP treatment introduced mechanical twins (MTs) to the brass surface layer, and the intersection of these MTs activated secondary twins during sliding. This process resulted in grain boundary expansion and grain refinement to the nanoscale. Furthermore, the yield strength of the worn brass with LSP was found to be improved by 2.81 times, enhancing the wear resistance of the brass.

Keywords Brass · Laser shock peening · Tribological behavior · Mechanical twins · Deformation mechanism

1 Introduction

Copper and its alloys are widely used in mechanical industries due to their excellent plasticity, machinability, and thermal conductivity [1–6]. The application of common components, such as bearings, gears, valves, and others, is widespread. However, these materials often exhibit relatively low strength and microhardness, which makes them susceptible to surface wear, particularly under harsh working conditions [7–10]. It is important to note that wear is a significant factor in the failure of approximately 80% of mechanical parts [11]. Such failures can lead to reduced work efficiency of equipment, increased maintenance costs, and even safety hazards. Therefore, it becomes crucial to perform surface treatment on brass to mitigate wear and extend the service life of components.

Common surface treatment techniques include chemical vapor deposition [12], thermal spraying [13], and laser

shock peening (LSP) [14–17] The spraying treatment requires a strong bond between the coating and the substrate, especially in high-temperature service conditions where the coating may be prone to peeling off. In contrast, LSP offers several advantages, including simplicity, environmental friendliness, and the ability to create a stable wear-resistant layer [18, 19]. Different from other surface treatment techniques, LSP treatment changes the microstructure and mechanical properties of the existing material without adding material to the surface. Recently, Ye et al. [20] provided an overview of the development of LSP for use in treating aircraft engine components over the past three decades. During the LSP process, pulsed laser light passes through a transparent restraining layer, such as a thin water layer or optical glass, and interacts with the metal material's surface. An absorbing coating, such as aluminum foil, black tape, or black paint, is applied to the metal's surface to absorb the laser energy and undergo instantaneous explosive vaporization, generating an ultra-high temperature (> 10,000 °C), high-pressure (> 1GPa) plasma. The presence of the restraining layer limits the expansion, resulting in the formation of a GPa-level instantaneous high-pressure shock wave in the metal's surface layer. In comparison to other surface treatment technologies like shot peening and ultrasonic impact peening [16, 21], LSP introduces high-density dislocations, nanotwins,

✉ Lin Liu
liulin@cczu.edu.cn

1 School of Mechanical Engineering and Rail Transit, Changzhou University, Gehu Zhong Road 21, Changzhou 213164, China

2 Institute for Technical Chemistry, Karlsruhe Institute of Technology (KIT), 76128 Karlsruhe, Germany

and other crystal defects into the surface layer through high-energy laser shock waves [22–24]. This results in higher stress and deeper penetration depth, leading to stronger and more uniform residual stress. Moreover, LSP offers the advantage of precise regulation of laser energy, pulse shape, spot size, and position, allowing treatment of areas that are difficult to address with conventional processes [25–28].

In recent years, Laser Shock Peening (LSP) has gained significant attention among researchers for enhancing wear resistance in metals and metallic alloys. For instance, Ye et al. [1] observed changes in copper's microstructure after Cryogenic Laser Shock Peening (CLSP) due to the effect of cryogenic temperatures. Wang et al. [29] investigated the impact of LSP on the wear resistance of brass and noted an increase in compressive residual stresses and microhardness with pulse intensity. Plastic deformation during LSP induces transformations in the surface layer's microstructure, which significantly influence the friction and wear behavior of contacting surfaces [30, 31]. However, the specific impact of microstructure evolution and deformation mechanisms on the tribological performance of metallic materials, especially copper alloys, with LSP treatment remains unclear. Therefore, a thorough understanding of how plastic deformation mechanisms, mediated by microstructure evolution, affect the tribological properties of copper alloys with LSP is essential. In addition, previous studies have investigated the running-in tribological behavior of brass and the formation mechanism of third bodies for brass under lubricated conditions [32, 33].

The objective of this study is to explore the effect of LSP on the microstructure evolution and deformation mechanisms of the worn layer in brass. Tribological experiments were carried out on both brass samples, one with LSP treatment and the other without LSP treatment, under Poly-alpha-olefin (PAO8) oil lubrication conditions using a tribometer. The worn morphologies are analyzed using scanning electron microscopy (SEM), while the grain distributions of the cross-sections in the worn layers are observed using the electron backscatter diffraction (EBSD) technique. Furthermore, the microstructures and strength of the brass surface layers are examined through transmission electron microscopy (TEM) and X-ray diffraction (XRD), respectively.

2 Experimental Procedures

2.1 Materials Preparation

The brass plates (COPPER MANUFACTURE, China) used in this study had a chemical composition consisting of 62.1% copper and 37.9% zinc, as indicated in Table 1. The performance parameters of the brass material are presented in Table 2. For achieving a uniform microstructure, an annealing process was conducted using a muffle furnace. The brass plates, with dimensions of 42 mm × 28 mm × 5 mm, were placed inside the furnace, and the heating components of the smelting furnace were adjusted to a temperature of 300 °C. The annealing process was carried out for 45 min, and then the furnace was cooled down gradually until the temperature reached room temperature. Subsequently, the furnace was discharged for air cooling of the brass plates. The brass plates underwent meticulous polishing to prepare their surfaces for further analyses. The polishing process involved using SiC paper with grit sizes of 600, 800, 1000, 1200, 1500, and 2000 # to remove any surface imperfections. This was followed by polishing with alumina suspension of 0.5 and 0.05 μm, respectively, to achieve a smooth and mirror-like finish on the brass surfaces. Finally, the plates underwent ultrasonic cleaning using an acetone solution to remove any contaminants adhered to the surface of the plates. Ultrasonic cleaning with absolute alcohol was performed for each sample, lasting 10 min. Following the cleaning process, the surface liquid was removed using cold air.

Table 2 Performance parameters of brass

σ_b/MPa	$\sigma_{0.2}$/MPa	E/GPa	Hardness/HV
372	230	124	100

Table 3 The parameters of LSP

Parameter	Value and unit
Laser pulse energy	7 J
Laser power density	9.06 GW/cm^2
Shockwave pressure	3.84 GPa
Laser pulse frequency	1 Hz
Laser pulse wavelength	1064 nm
Laser pulse width	10 ns
The beam diameter	3 mm
Overlapping rate	50%

Table 1 Chemical composition of the brass plates (mass fraction, %)

Cu	Fe	Pb	Zn
60.5~63.5	≤0.15	≤0.08	Bal

2.2 Laser Shock Peening

The laser shock peening (LSP) experiments were conducted using an Nd: YAG high-power laser system (Coherent, Inc.). The specific parameters used for LSP are presented in Table 3. In order to enhance the efficiency of LSP, an aluminum foil with a thickness of 0.1 mm was chosen as the absorbing layer, while a layer of running water with a thickness of 1.0 mm served as the transparent confining layer. The area and scanning path for the LSP treatment are illustrated in Fig. 1. The laser intensity (E_{laser}) of the laser, with a unit of GW/cm^2, can be calculated using the following formula Eq. (1) [34]:

$$I_0 = \frac{4\chi E_{laser}}{\pi \tau D^2} \tag{1}$$

where E_{laser} represents the intensity of the laser, D represents the beam diameter. χ represents the absorption coefficient of the absorption layer, the value is 0.6. Based on the above parameters, the intensity of laser is 9.06 GW/cm^2.

Base on Fabbro's model, the shockwave pressure can be calculated by the following formula Eq. (2) [34]:

$$P_{max} = 0.01\sqrt{\frac{\alpha}{2\alpha + 3}}\sqrt{Z}\sqrt{I_0} \tag{2}$$

where I_0 is the laser intensity, α is the interaction efficiency (which is typically calculated at 0.15). Z is the shockwave impedance of the material. In order to calculate the value of Z, the following formula Eq. (3) was employed [35]:

$$\frac{2}{Z} = \frac{1}{Z_1} + \frac{1}{Z_2} \tag{3}$$

where Z_1 and Z_2 represent the acoustic impedance of the material and confinement media. Based on the above formula, the shockwave pressure can be calculated and the final value is 3.84 GPa.
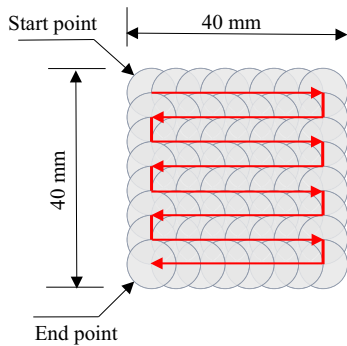

Fig. 1 The area and scanning path of LSP

2.3 Tribological Experiment

Tribological tests were carried out using the Rtec Universal Tribometer (RTEC MFT-50) (Rtec-Instruments, the USA). The sliding contact was established between the selected balls (made of E52100 alloy steel) with a diameter of 5.0 mm and a hardness of 63 HRC, and the surface of the brass plates. The tests were performed under the following conditions: lubrication with PAO-8 oil [33], room temperature (25°C), point-to-point contact between the friction pairs. The test parameters included a rotary radius of 8 mm, sliding speed of 60 r/min, and a total testing time of 45 min. The normal loads applied during the experiments were as follows: 5.0 N, 8.0 N, 12.0 N, 20.0 N, and 40.0 N. To ensure the accuracy of the experimental data, each test was repeated three times under identical working conditions. The friction coefficients were determined by calculating the average value and the corresponding standard deviation.

2.4 Microstructure Observation

The worn surface morphologies were observed using a scanning electron microscope (SEM) (JSM-6510) (JEOL, Japan). Energy-dispersive X-ray spectroscopy (EDS) was employed for chemical composition analysis of the worn surface. Point analysis was performed to obtain the elemental composition of the samples. Cross-sectional views of both LSP-treated and untreated brass samples after sliding were obtained using electron backscatter diffraction (EBSD) on a Sigma 500-FESEM (Zeiss, Germany). Prior to EBSD observation, the samples were polished using an electrolytic polisher at room temperature. The electrolytic polishing solution consisted of H_3PO_4: H_2O: CH_3CH_2OH in a ratio of 2:1:1. The applied voltage and time for electrolytic polishing were 10 V and 30 s, respectively.

The surface roughness of the brass was measured using a 3D Optical Profiler (Contour-GT) (Bruker, the USA) with a resolution of 100 nm. In order to ensure the accuracy of data, the tests were repeated 3 times. Transmission electron microscopy (TEM) (JEOL 2100, Japan) was utilized to examine the microstructure of the worn surface layers. TEM samples were prepared by single-spray thinning using a twin-jet electro-polisher (TenuPol-5) (Struers, France) to obtain detailed microstructural information from the worn surfaces. The electrolytic solution used was CH_3OH:HNO_3 in a ratio of 2:1. X-ray diffraction (XRD) experiments were performed using a D/max2500 device (Rigaku, Japan) with Cu K_α radiation ($\lambda = 0.154051$ nm). The scanning was conducted in the 2θ range of 20°–90° with a step size of 0.02°. The speed of scanning is 4 degree/min. The XRD device operated at 40 kV and 150 mA.

3 Results and Discussion

3.1 Tribological Behaviors

The variations in friction coefficients obtained from the sliding tests for brass with and without LSP are illustrated in Fig. 2. For brass without LSP, the friction coefficients are 0.18 ± 0.02, 0.26 ± 0.08, 0.27 ± 0.03, 0.32 ± 0.04, and 0.39 ± 0.07, respectively, when the normal loads are 5.0 N, 8.0 N, 12.0 N, 20.0 N, and 40.0 N. It is evident that the friction coefficient increases with the increment of the normal load. The rise in the friction coefficient can be attributed to the increased frictional stress within the contact pair due to the higher normal load, resulting in accelerated wear of the brass without LSP.

In contrast, for the LSP-treated specimens, the friction coefficients are 0.16 ± 0.03, 0.25 ± 0.08, 0.20 ± 0.02, 0.15 ± 0.01, and 0.40 ± 0.04, respectively, when the normal loads are 5.0 N, 8.0 N, 12.0 N, 20.0 N, and 40.0 N. The behavior of friction coefficients differs from that of brass without LSP as the normal load increases. Notably, when the normal load is 20.0 N, the mean value and standard deviation of the friction coefficient are the lowest, indicating a good contact and stable sliding test conditions. This can be attributed to the introduction of regularly arranged micro-pits on the surface layer of LSP-treated brass, which allows for the storage of lubricating oil within the micro-pits. The standard deviations are large under other conditions, which can be influenced by surface roughness, hardness, wear debris or lubrication. As the sliding test progresses, the lubricating oil is continuously supplied to the contact area between the brass and

the grinding ball, thereby providing secondary lubrication [36]. Consequently, the friction coefficient of brass with LSP decreases. Additionally, the limited presence of lubricating oil at the contact interface causes it to quickly overflow under the influence of extrusion as the load increases. Consequently, the contact area between the upper and lower specimens also increases, leading to a rapid rise in the friction coefficient and resulting in lubrication failure. This observation aligns with previous studies, where it was found that the friction coefficient increases notably when the normal load reaches 40 N [36, 37]. As depicted in Fig. 2b, it is evident that the brass surface roughness with LSP is measured to be 3.95 μm, which is higher compared to the surface roughness without LSP. This increase in roughness can be attributed to the surface plastic deformation induced by the high-pressure shock waves during LSP treatment. However, after the completion of the sliding test, the surface roughness for both samples, with and without LSP, appears to converge and become relatively similar.

To further differentiate the tribological performance between the two conditions, a normal load of 20.0 N was selected for the experiment. The friction coefficient versus cycles for brass with and without LSP is presented in Fig. 3a. For brass without LSP, the friction coefficient shows a gradual increase during the initial stage (approximately the first 1000 cycles) due to proper contact of the original friction pairs. Subsequently, from 1000 to 2500 cycles, the friction coefficient further increases from 0.21 to 0.25. Eventually, it stabilizes at around 0.24. Figure 3c shows the SEM image of the worn surface of brass without LSP, revealing the presence of pits and cracks. The brass surface experiences abrasive wear, with abrasive debris particles being detached and
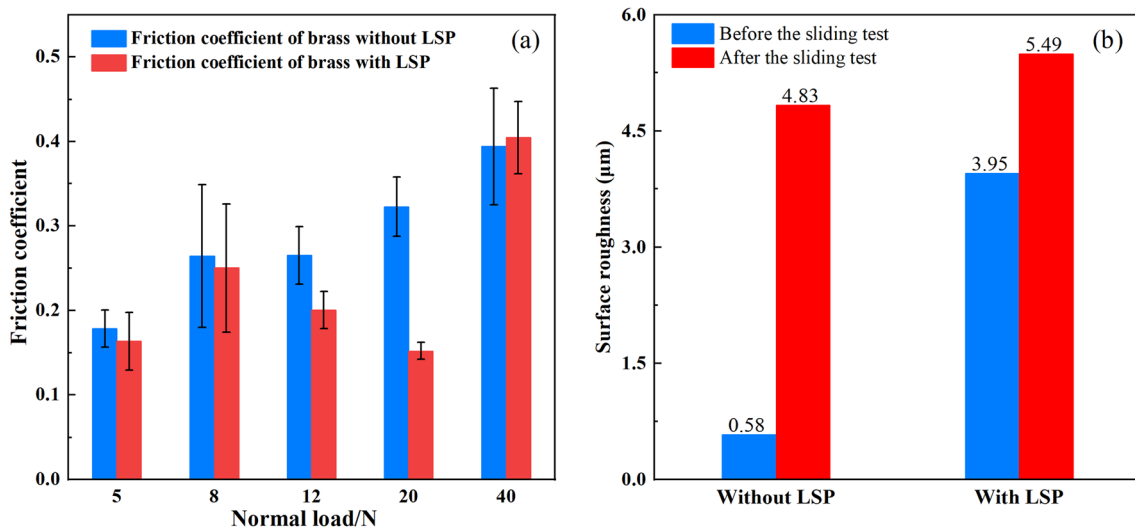

Fig. 2 **a** Friction coefficient of brass with and without LSP under different normal loads; **b** the surface roughness when the normal load is 20 N
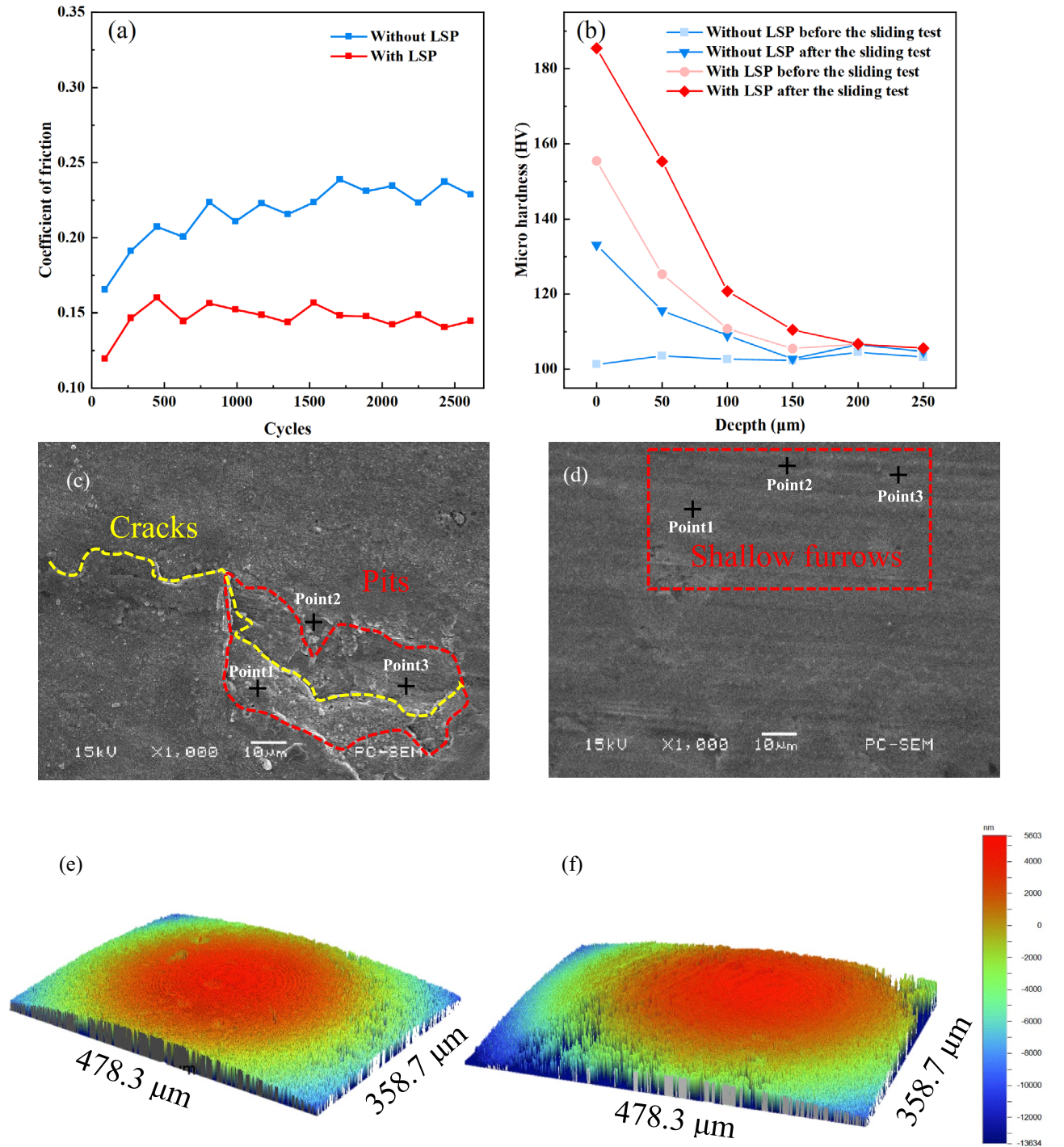
Fig. 3 **a** Friction coefficient without and with LSP; **b** Micro hardness curves of specimens along the cross-section SEM images of worn surface for the plates **c** without and **d** with LSP; **e** the surface topography of counter ball and **f** the surface topography of the worn counter ball

peeled off. The severe damage is caused by the ploughing action of the steel ball, as shown in Fig. 3d. These observations indicate that fatigue wear is one of the primary wear mechanisms for brass without LSP. As depicted in Fig. 3e and f, it is evident that the surface topography of the brass

after the sliding test is notably different from its initial state before the test, as it appears rough and non-smooth. Additionally, EDS analysis of the worn surface in Fig. 3c reveals the presence of Fe elements (as shown in Table 4), indicating material transfer between the friction pairs and the

Table 4 EDS analysis of worn surface for the plate without LSP

Element	Mass %	Error %	At %
C	2.10	0.10	10.06
O	1.77	0.10	3.76
Fe	2.59	0.51	2.61
Cu	62.65	1.43	56.63
Zn	30.89	2.03	26.94
Total	100.00		100.00

Table 5 EDS analysis of worn surface for the plate with LSP

Element	Mass %	Error %	At %
C	5.67	0.11	23.74
O	1.00	0.12	3.14
Cu	61.60	1.03	48.73
Zn	31.72	2.32	24.39
Total	100.00		100.00

occurrence of adhesive wear. The combined effect of these two wear mechanisms exacerbates poor contact between the friction pairs, leading to sharp fluctuations in the friction coefficient during the second stage. Ultimately, a dynamic equilibrium is established in terms of the generation, peeling, and transfer of wear debris particles, signifying the attainment of a stable state during the sliding running-in process. On the other hand, the friction coefficient of brass with LSP, represented by the red line in Fig. 3(a), exhibits a favorable running-in behavior. In the first 500 cycles, the friction coefficient slightly increases to 0.16 and then remains consistently around 0.15 until the end of the test. The average friction coefficient value of 0.15 is significantly lower than that of brass without LSP.

The findings shows that the friction pairs are in good contact during the tribological process. According to Fig. 3d, the worn surface of brass with LSP is overall flat. Moreover, only a few shallow furrows are observed on the worn surface and no element transfer between the friction pairs is found by EDS analysis as Table 5 displayed. We suspect that the main wear mechanism of brass with LSP is abrasive wear. Compared with the tribological behaviors of brass with and without LSP treatment, the brass with and without LSP treatment exhibit distinguished different wear mechanisms during the sliding test, the surface of brass with LSP is strengthened obviously. Moreover, the results imply that the strengthened brass surface has an excellent ability to resist external force deformation and the brass with LSP presents better tribological behaviors during the tests.

These results indicate that the friction pairs maintain good contact during the tribological process. As shown in Fig. 3d, the worn surface of brass with LSP appears overall

flat. Additionally, only a few shallow furrows are observed on the worn surface, and EDS analysis (as shown in Table 5) does not reveal any element transfer between the friction pairs. This suggests that the main wear mechanism for brass with LSP is abrasive wear. A clear distinction in wear mechanisms is observed between brass with and without LSP treatment during the sliding test, with the surface of brass with LSP exhibiting significant strengthening. As shown in Fig. 3b, before the sliding test, the hardness of the brass surface increased from 100 to 136 after undergoing LSP treatment. Following the sliding test, the hardness further increased from 136 to 183 with LSP. Notably, compared to the brass without LSP, it is evident that LSP significantly enhances the working hardening ability of the brass surface. Furthermore, the results imply that the strengthened surface of brass with LSP demonstrates excellent resistance to external force deformation, resulting in improved tribological performance during the tests.

3.2 EBSD Analysis

As depicted in Fig. 4a and d, the change in grain color indicates a significant alteration in the grain orientation on the surface of brass when subjected to LSP. Evidently, a substantial number of twins are introduced into the brass surface during LSP treatment. The resulting strengthening layer measures 62.5 μm in thickness. Figure 4b and e demonstrate that the fraction of grains with sizes smaller than 20 μm increases from 5.31 to 26.76% after LSP treatment. Similarly, Fig. 4c and f reveal an increase in the fraction of low-angle grain boundaries from 10.13 to 23.12%. This suggests that LSP effectively refines the surface grains of brass. After the wear tests, the fraction of grains with sizes smaller than 20 μm further increases from 26.76 to 88.79%, as illustrated in Fig. 4e and k. Additionally, the fraction of low-angle grain boundaries increases from 23.12 to 43.75%. These results indicate that the surface grains of brass undergo further refinement after wear testing.

In the worn layer of brass without LSP, as depicted in Fig. 4g, different grain textures are distributed. Based on the grain size distribution, the worn layer can be divided into two regions: the severe plastic deformation (SPD) layer and the minor plastic deformation (MPD) layer. The thicknesses of these layers are measured to be 60.5 μm and 144.5 μm, respectively. After the sliding test, the grain sizes in the SPD layer and MPD layer are refined to approximately 30 μm and 40 μm, respectively. A similar observation is made in the worn layer of brass with LSP, as shown in Fig. 4j, where the thicknesses of the SPD layer (with an average grain size of 20 μm) and the MPD layer (with an average grain size of 25 μm) are found to be 77.3 μm and 88.3 μm, respectively. Figure 4h and k show that the fraction of grains with sizes smaller than 20 μm increases from 43.34 to 88.79%.
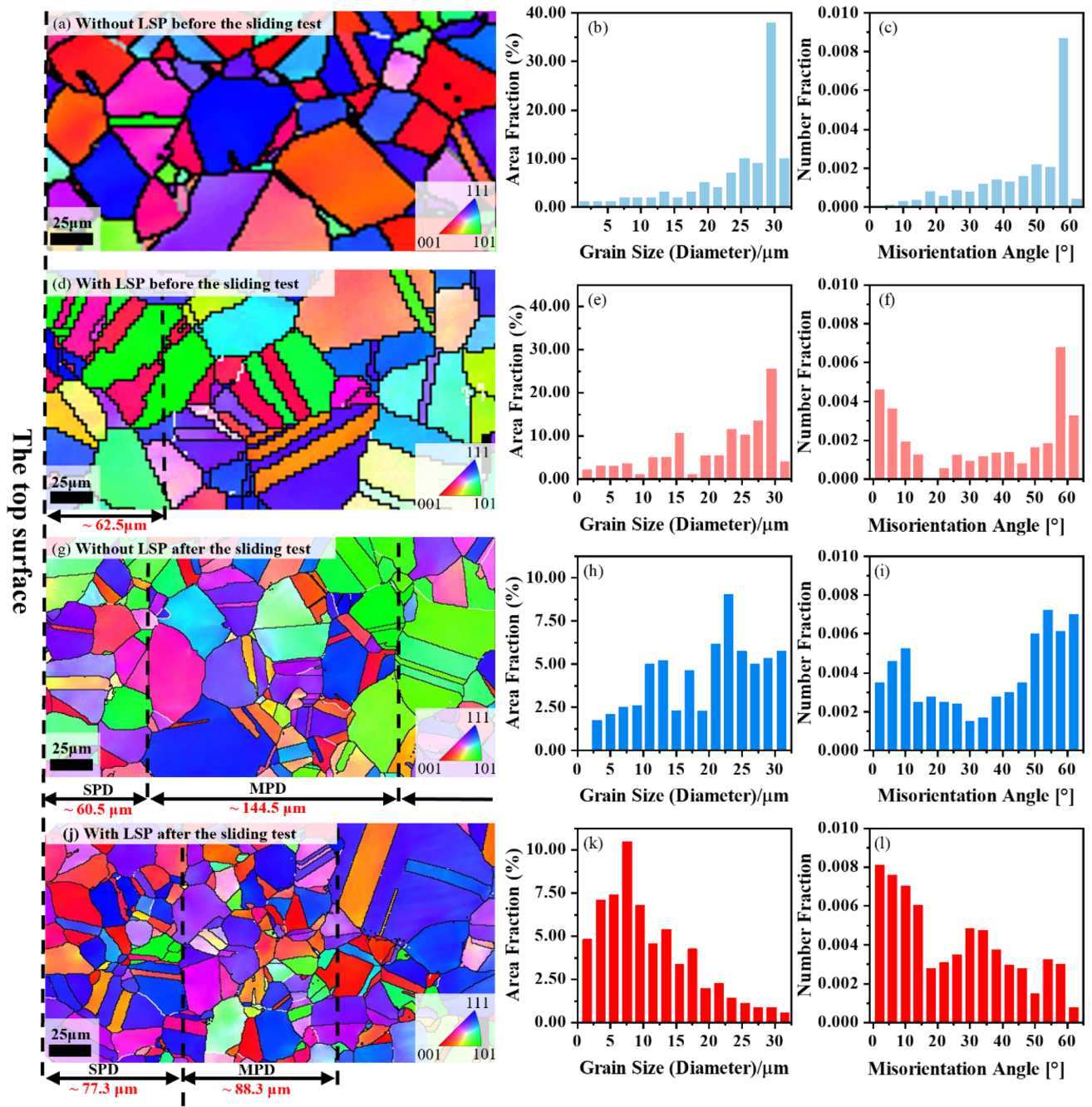
Fig. 4 EBSD results of inverse pole figure (IPF), grain size and grain boundary misorientation. **a**, **b** and **c** for the top layer of the plate without LSP before the sliding test; **d**, **e** and **f** for the top layer of the plate with LSP before the sliding test; **g**, **h** and **i** for the worn layer of the plate without LSP after the sliding test; **j**, **k** and **l** for the worn layer of the plate with LSP after the sliding test

Additionally, the fraction of low-angle grain boundaries (LABs), which correspond to low misorientation angles less than 15°, increases from 25.43 % (Fig. 4i) to 43.75% (Fig. 4l).

The thickness of the worn layer is measured to be 205.0 μm for brass without LSP and 165.6 μm for brass with LSP. The worn layer in brass with LSP is 39.4 μm thinner

compared to brass without LSP. This phenomenon can be attributed to the grain refinement effect caused by the laser shock wave, which enhances the strength of brass. Previous studies by Mao et al. [38] have shown an inverse relationship between wear resistance and grain size in the worn layer. Therefore, the nanometer-sized grain refinement results in significant strengthening of the metal, leading to improved

wear resistance. The LSP treatment enhances the wear resistance of brass, which is consistent with the results obtained from the tribological tests.

3.3 TEM Observation

3.3.1 Microstructure of the Worn Layer for Brass Without LSP

In the microstructure of the worn layer for brass without LSP, several dislocation lines (DLs) ranging from 10 to 100 nm in length can be observed, as shown in Fig. 5a. These DLs have a random distribution on the worn surface. The accumulation of these DLs leads to the formation of high-density dislocation tangles (DTs), as seen in Fig. 5b, and dislocation cells (DCs), as seen in Fig. 5c, with sizes ranging from 200 to 300 nm. Similar findings have been reported by Lou et al. [39]. Furthermore, the DCs are found to be distributed along the boundaries. Figure 5d shows that the boundaries of the original DCs are interconnected,

forming smaller subgrains with a size of approximately 200–300 nm.

3.3.2 Microstructure of the Worn Layer for Brass with LSP

Before the sliding test, the surface layer of brass with LSP exhibits two distinct stacking faults (SF_1 and SF_2) around the original grain boundaries (GBs), as indicated by the yellow dotted line in Fig. 6a and b. Additionally, several clusters of parallelly arranged mechanical twins (MTs) can be observed along the original GBs. As shown in Fig. 6a, the MTs are blocked by the GBs at an angle θ_1 of approximately 53° between the MTs and the grain boundary.

As the sliding test commences, the stacking faults (SF_3) in Fig. 7a diminish. However, with the increasing number of MTs, they start to cross the original GBs (yellow dotted line) in Fig. 7a. Once the MTs cross the original GBs, they continue to expand along with the movement of dislocations. Figure 7b illustrates the high density of dislocations distributed in area A and area B, with the MTs still aligned parallel

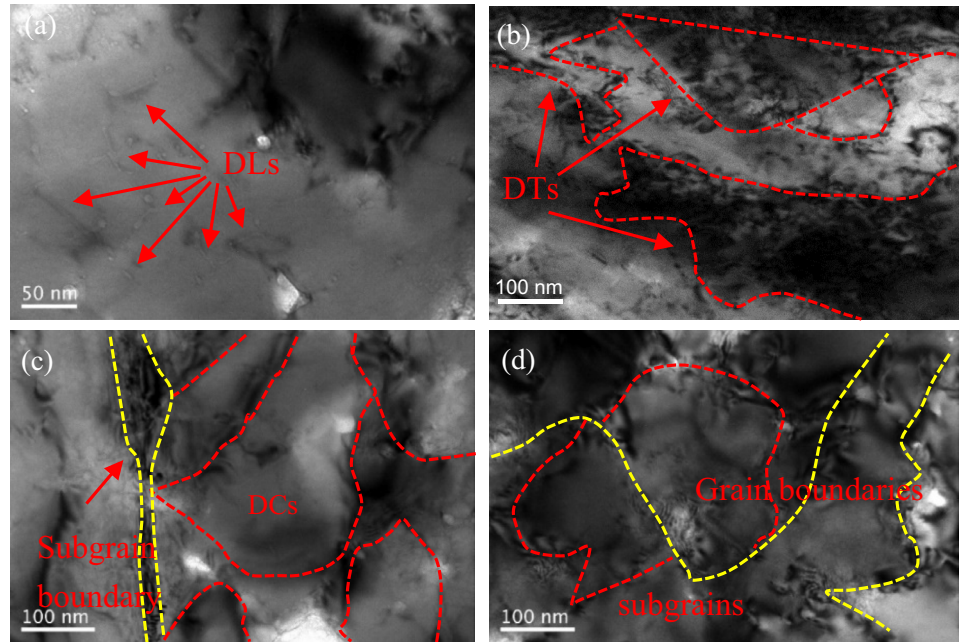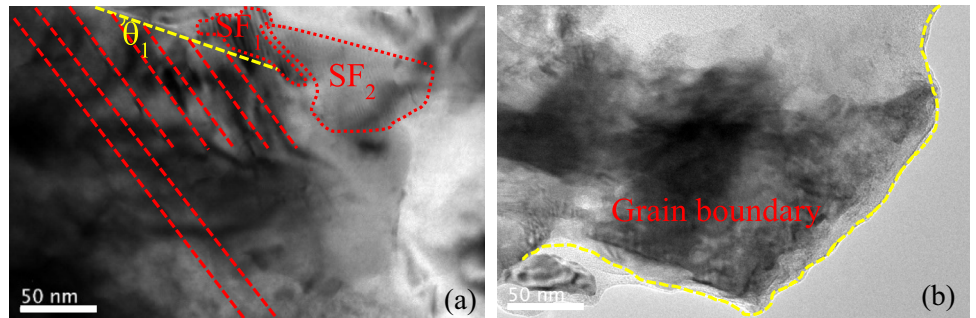**Fig. 5** TEM images of the worn surface layer for the plate without LSP

Fig. 6 TEM images of the worn surface layer for the plate with LSP before the sliding test. **a** Staking faults, **b** grain boundary
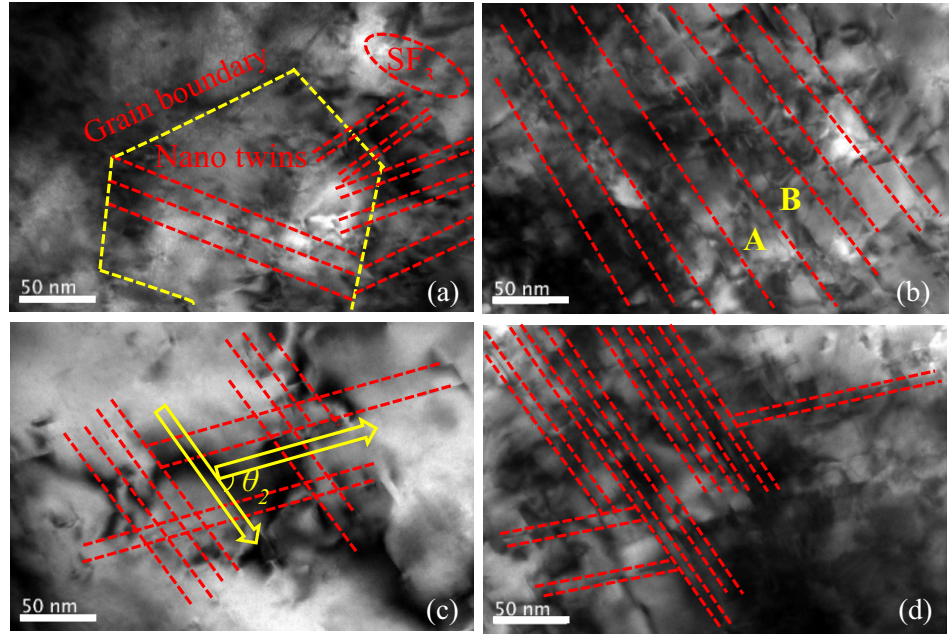
Fig. 7 MTs and the finer twins of the worn surface layer for the plate with LSP after the sliding test. Interaction of the MTs and GBs for surface layer of the plate with LSP can be observed. **a** MTs cross GBs when sliding test finished; **b** MTs; **c** MTs cross each other; **d** finer twins

to each other. As the MTs of different directions expand during sliding, intersecting MTs begin to emerge, as depicted in Fig. 7c. The crossing angle between the MTs, denoted as θ_2, measures approximately 70°. Moreover, a high density of dislocation structures can be observed at the intersection of MTs in Fig. 7c. Furthermore, finer twins oriented in different directions are present in Fig. 7d, and the spacing between twins in the same direction is approximately 10 nm.

In addition, the spacing between the finer twins increases with the sliding test commencing, as shown in Fig. 8a. The MTs and finer twins intersect and cut through the dislocation cells, resulting in the formation of subgrains. Subsequently, these subgrains undergo a transformation into nanograins through dislocation movements occurring between the MTs and finer twins. Figure 8b demonstrates that the average grain size is approximately 80–90 nm, and the angle θ_3 measures around 60°, which falls between the grains with a size of approximately 100 nm within the red rectangular region.

3.4 Plastic Deformation Mechanisms of the Worn Layer for Brass

3.4.1 XRD Analysis

Based on the previous analysis, it is evident that subgrains and nanograins are present in the final state of the worn layers for brass without LSP and with LSP, respectively. Furthermore, the tribological performance of brass with LSP is superior to that of brass without LSP. The classic Hall–Petch relationship [40] suggests that the yield strength is influenced by both dislocation density and grain size. To further investigate the impact of yield strength on the tribological behavior of brass, the dislocation density of the worn surface was examined through XRD experiments.

Figure 9 displays the diffraction patterns of the main crystal planes {111}, {200}, {220}, and {311}. Utilizing the G. K. Williamson equation [41], the dislocation density can be calculated using Eq. (4):

Fig. 8 The formation of nanograins of the worn surface layer for the plate with LSP after sliding test. **a** MTs and the finer twins cut dislocation cells; **b** nanograins
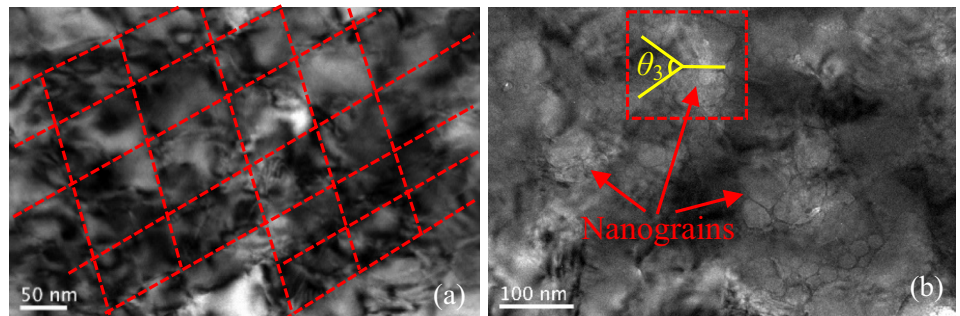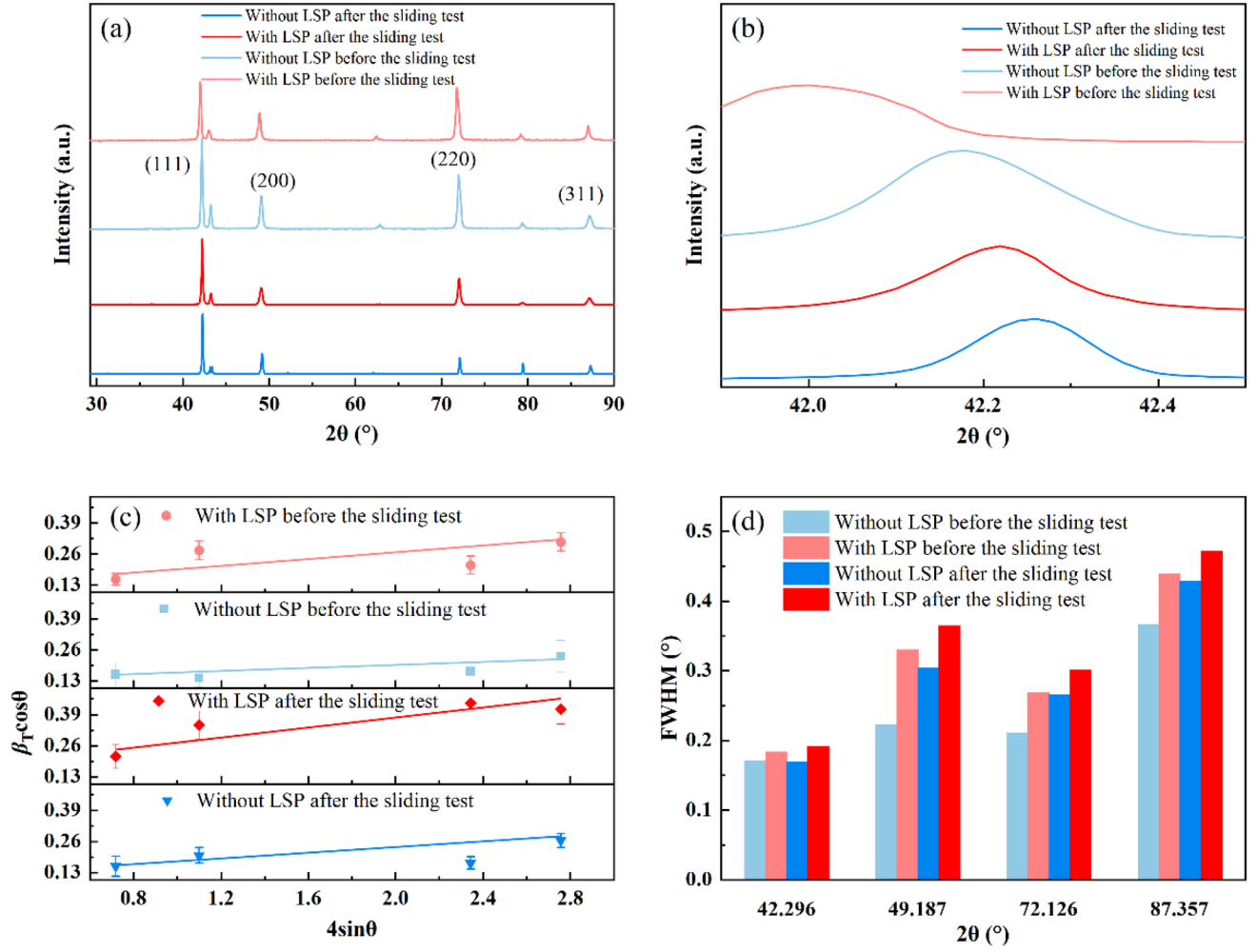
Fig. 9 the brass of **a** XRD analysis; **b** magnification drawing within certain range of 41.5°—42.5° of XRD patterns **c** Williamson—Hall analysis; **d** FWHM analysis

$$\rho_d = \frac{2\sqrt{3}\langle\varepsilon^2\rangle^{1/2}}{d_{XRD}b} \tag{4}$$

where ρ_d is the dislocation density, ε is strain, d_{XRD} is the grain size by XRD analysis, and b is Burger's vector with a value of 0.3 nm for brass [42].

After performing fitting calculations using Jade software, the grain sizes (d_{XRD}) of brass with and without LSP are determined to be approximately 1601.30 nm and 940.10 nm, respectively. The strains (ε) exhibited are approximately 0.11 and 0.03, respectively. Consequently, the dislocation densities of the brass with and without LSP before the sliding test are estimated to be around 1.36×10^{15} m^{-2} and 2.17×10^{14} m^{-2}, respectively. Additionally, the grain sizes (d_{XRD}) of the worn layers for brass with and without LSP are determined to be approximately 174.60 nm and 109.70 nm, respectively.

The strains (ε) exhibited by the worn layers are approximately 0.06 and 0.19, respectively. Consequently, the dislocation densities of the worn layers are estimated to be around 3.77×10^{15} m^{-2} and 1.96×10^{16} m^{-2}, respectively. In this study, Fig. 9d illustrates the change in FWHM for all tested brass samples. It is evident that LSP increases the dislocation density of brass. Furthermore, it has been observed that the dislocation density of brass increases even further after wear, compared to its state before the sliding test. The dislocation density of the worn layer with LSP is found to be 5.19 times higher than that of the worn layer without LSP. This increase in dislocation density enhances the yield strength of the surface layer, thereby improving the wear resistance of brass.

In order to calculate the yield strength of the worn layers for brass with and without LSP, N.K. Kumar et al. [43] Eq. (5) is performed.

$$\sigma_y = \sigma_0 + k(\frac{1}{d_{twin}} + \frac{1}{d_{XRD}})^{1/2} + \alpha Gb\sqrt{\rho_d} \qquad (5)$$

where σ_0 is initial yield strength with a value of 230 MPa, k is Hall–Petch slope with a value of 16 MPa.mm$^{1/2}$, α is constant with a value of 0.2, G is the elastic modulus with a value of 39 GPa [42], and d_{twin} is the average twins size,. d_{XRD} for the worn layers of brass with and without LSP are 174.60 nm and 109.70 nm by the XRD analysis respectively. This is consistent with the results from TEM observation. d_{twin} for the worn layer of brass with LSP is 20 nm by TEM. While d_{twin} for the worn layer of brass without LSP is zero because no twins were observed by TEM. The average value of ρ_d increases from 3.77×10^{14} up to 1.96×10^{16} m^{-2} by XRD analysis. Finally, the σ_y grows from 159.19 up to 449.52 MPa. The yield strength(σ_y) of the worn layer for brass with LSP improves by 2.81 times compared with that of the worn layer without LSP. The increase + in yield strength enhances the ability to resist brass deformation caused by an external force, which also confirms the analysis results in Sect. 3.2.

3.4.2 Plastic Deformation Mechanism of the Worn Layer for Brass Without LSP

To further understand the microevolution process of the worn layer in brass without LSP, a schematic illustration of the microstructure evolution mechanism is presented in Fig. 10.

(I)　The initial stage of microstructure evolution in the surface layer of brass without LSP is depicted in Fig. 10a, where the original grains are shown. At this stage, the dislocations are randomly distributed within the original grains.

(II)　As the sliding test progresses, the friction stress causes the accumulation of dislocations, forming dislocation lines (DLs) as observed in Fig. 5a. This accumulation of dislocations is illustrated in Fig. 10b. The microstructure evolution of the surface layer enters stage II.

(III)　With the sliding test continuing, the wear between the brass and grinding ball intensifies. The annihilation and rearrangement of DLs give rise to the formation of dislocation tangles (DTs) (Fig. 5b), as depicted in Fig. 10c. Under the influence of friction stress, the higher density of DTs gradually interconnects to form dislocation cells (DCs) (Fig. 5c).

Fig.10 Schematic illustration of the microstructural evolution for the worn surface layer of brass without LSP during sliding. **a** the initial grains before sliding, **b** DLs, **c** DTs and DCs, **d** subgrains
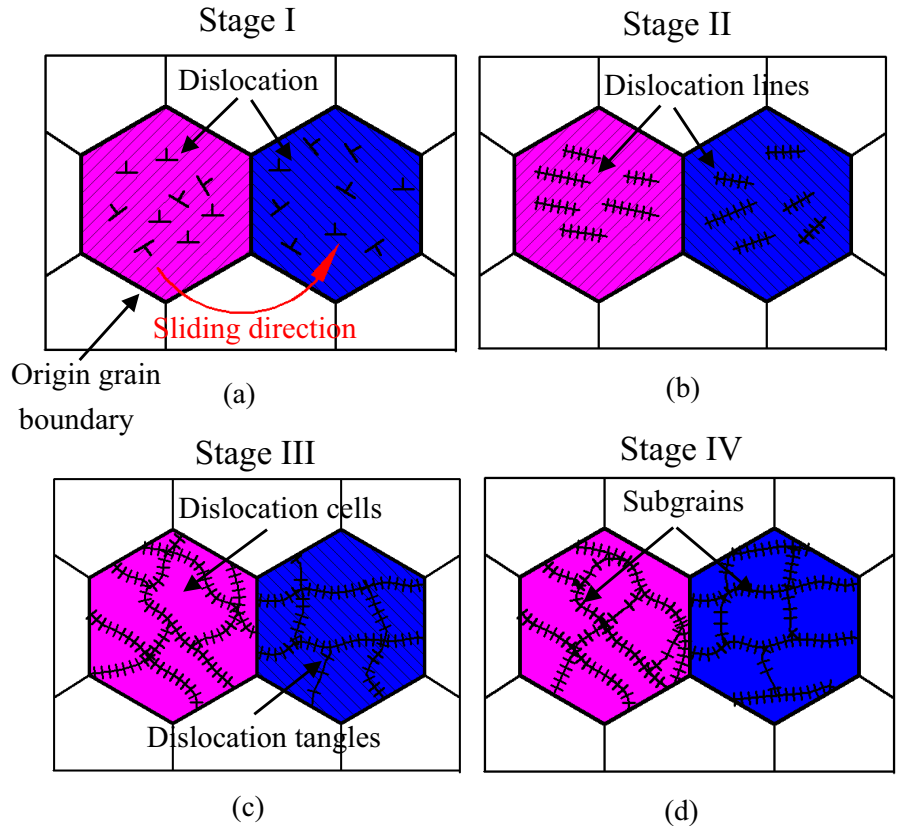
(IV) In the final stage, the interaction between DTs and DCs strengthens, leading to the development of subgrains (Fig. 5d), as shown in Fig. 10d. Subgrains are unstable microstructures, particularly with weak inhibition of subgrain boundaries on dislocation movement. This results in a lower yield strength of the worn surface layer in brass without LSP. Consequently, the generation of subgrains indicates the instability of the microstructure in the worn layer, contributing to ploughing of the layer.

By understanding the microstructure evolution mechanism, it becomes evident that the absence of LSP treatment in brass leads to the formation of unstable subgrains and a weakened surface layer, ultimately affecting the wear resistance of the material.

When considering the results presented in Sect. 3.1, it can be observed that in the final stage of the sliding test (1890–2700 cycles), the friction coefficient of brass without LSP is high, and larger pits and cracks are evident on the worn surface. These phenomena can be attributed to the presence of unstable subgrains in the surface layer, which lead to reduced strength and a diminished load-bearing capacity. Consequently, the high friction coefficient and the occurrence of numerous pits and cracks on the worn surface are a direct consequence of these unstable subgrains.

During the sliding test, the main deformation mechanism in brass without LSP is dislocation slip. However, the dominance of this deformation mechanism, characterized by dislocation slip, is associated with poor tribological behavior in the brass without LSP. The unstable subgrains, resulting from the accumulation and rearrangement of dislocations, contribute to the unfavorable tribological characteristics observed.

Therefore, the presence of unstable subgrains and the prevalence of dislocation slip as the primary deformation mechanism lead to diminished strength, poor load-bearing capacity, and ultimately, unsatisfactory tribological behavior in brass without LSP.

3.4.3 Plastic Deformation Mechanism of the Worn Layer for Brass with LSP

To gain further insight into the microevolution process of the worn layer in brass with LSP, a schematic illustration of the microstructure evolution mechanism is presented in Fig. 11. This illustration takes into account the analysis of the typical tribological behaviors described in Sect. 3.1, as well as the observed microstructure changes discussed in Sect. 3.2 and 3.3, throughout the sliding test.

(I) Prior to the sliding test, dislocation movements are initiated as a result of the LSP treatment. LSP, as a surface strengthening technique, induces an ultra-high strain rate on the surface layer of the substrate. The energy generated from this ultra-high strain rate activates partial dislocations, leading to the generation of MTs [44]. This observation aligns with our previous findings [45]. As depicted in Fig. 11a, the original grains are refined into twin-substrate lamellae through the action of MTs during the initial stage. Furthermore, these MTs are

Fig. 11 Schematic illustration of the microstructural evolution for worn surface layer of the plate with LSP. MTs distribution before sliding (**a**), MTs crossing GBs (**b**), MTs intersection (**c**), the formation of secondary twins (**d**), the formation of subgrains (**e**), the formation of nanograins (**f**)
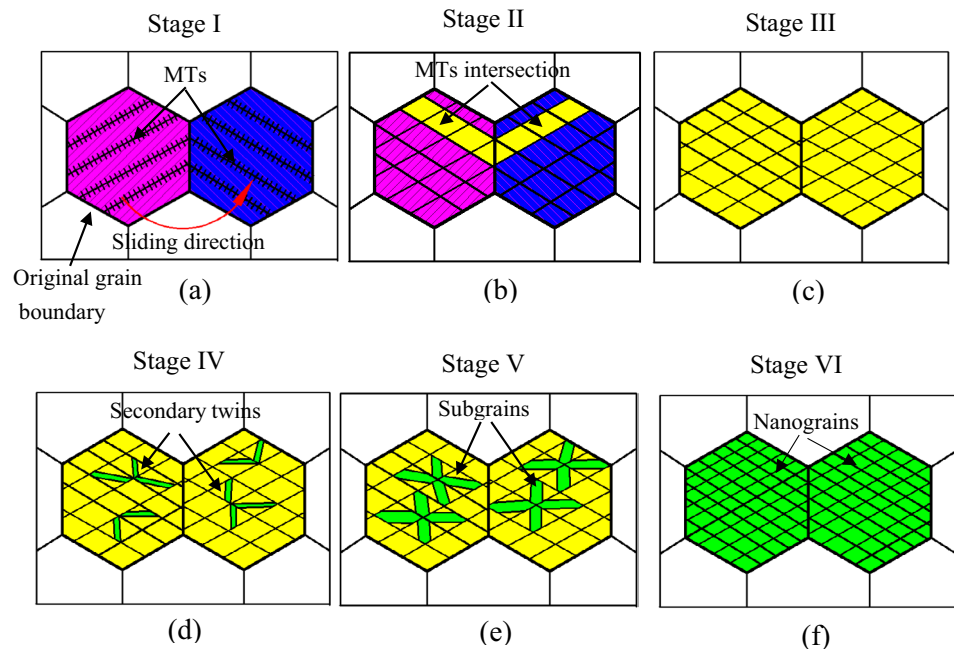
distributed along the original grain boundaries and are impeded by the presence of these boundaries. Consequently, the original grains on the surface layer of brass with LSP undergo initial refinement due to the influence of MTs.

(II) In stage II, as the sliding test commences, the MTs gradually penetrate the barrier posed by the original grain boundaries (Fig. 7a) and cross over these boundaries, as illustrated in Fig. 11b. During stage I, although LSP promotes the formation of MTs, it does not provide sufficient driving force for the MTs to overcome the barrier imposed by the original grain boundaries in brass. This occurs because the driving force generated by the LSP treatment alone is insufficient to facilitate the crossing of MTs over the original GBs. However, as the sliding motion initiates, the interaction between the MTs and grain boundaries becomes more pronounced. When the driving force accumulates to a certain intensity, the MTs successfully break through the barrier of the original grain boundaries. Subsequently, the MTs continue to expand forward after crossing over these boundaries. Whenever the expansion of MTs encounters stress concentration, a new expansion direction is activated. As the sliding motion progresses, the MTs expand in different directions, working in conjunction with one another and accelerating the refinement of grains. The new refined MTs are represented by the yellow diamond in Fig. 11b. These new MTs are formed through the cutting of the original grains in brass by the crossed MTs.

(III) In stage III, the process of MTs crossing continues under the influence of friction (Fig. 7b and c), gradually completing the cutting of the original grains. The newly refined grains in the worn surface layer of brass with LSP are depicted in Fig. 11c, where the yellow diamonds represent the newly refined grains. In this stage, compared to stages I and II, the boundaries of MTs in the worn surface layer of brass with LSP significantly increase. These MTs boundaries hinder the movement of dislocations, leading to the accumulation of dislocations at the MTs boundaries. Notably, due to the high dislocation density, a substantial amount of strain energy is stored at the intersections of MTs.

(IV) In stage IV, the high-density dislocation structures at the intersections of MTs (Fig. 7c) result in a highly energetic and unstable state of the system [46]. To lower the system's energy, the dislocations at the MTs intersections undergo rearrangement and form new boundaries, triggering the formation of finer twins (Fig. 7d), also referred to as sec-

ondary twins. The green quadrilaterals in Fig. 11d represent these secondary twins. The formation of secondary twins is progressively stimulated in stage IV. The grains in the worn surface layer of brass with LSP undergo further refinement, and the boundaries of secondary twins continue to expand. This restricts the region where dislocations can move freely within the grain, leading to shorter dislocation-free paths. Moreover, the length of the dislocation-free path is inversely correlated with the yield strength[47]. As the free path of dislocations becomes shorter, the yield strength of the worn surface layer of brass with LSP improves. Consequently, due to the strengthening effect of MTs and secondary twins, the worn surface layer of brass with LSP exhibits excellent wear resistance when subjected to friction. These findings are consistent with the observations in Sect. 3.3. The exceptional wear resistance of brass with LSP results in a reduced total depth of plastic deformation in the worn layer under identical sliding test conditions compared to brass without LSP.

(V) In stage V, as the sliding test progresses, the number of secondary twins gradually increases, further accelerating the process of grain refinement. The original grains in the surface layer of brass with LSP are gradually transformed into subgrains (Fig. 8a), as illustrated in Fig. 11e.

(VI) In the final stage, under the influence of friction, the subgrains gradually interconnect, forming additional new grain boundaries (Fig. 8b). At these new grain boundaries, dislocations undergo annihilation and rearrangement, resulting in the formation of nanograins with sizes ranging from 80 to 100 nm, as shown in Fig. 11f. Nanograins are microstructures known for their excellent mechanical properties. Studies by Lu. K [48] have demonstrated that nanograins can significantly enhance the strength and hardness of metals. Combining these findings with the observations in Sect. 3.1, it becomes evident that the wear mechanisms in brass without LSP involve fatigue wear and adhesive wear, whereas in brass with LSP, abrasive wear dominates. The presence of LSP imparts good wear resistance to the brass.

In summary, deformation twinning, including the formation of MTs and secondary twins, serves as the primary deformation mechanism for the worn layer of brass with LSP during sliding. As MTs and secondary twins develop, grain boundaries grow, leading to the gradual refinement of grains into nanograins. This refinement process contributes to the enhanced wear resistance of brass with LSP.

4 Conclusion

In this study, we conducted a systematic investigation into the influence of laser shock peening (LSP) on the microstructure evolution and deformation mechanism of the worn layer in brass. The key findings and conclusions are summarized as follows, which provide valuable insights into the tribological performance of brass and the effects of LSP:

(i) Superior tribological behaviors with LSP: The brass subjected to LSP exhibited superior tribological performance compared to the brass without LSP. Firstly, the wear mechanisms differed significantly between the two conditions. The brass without LSP experienced fatigue and adhesive wear, resulting in the formation of pits and cracks on the worn surface. In contrast, the brass with LSP primarily underwent abrasive wear, characterized by a reduced occurrence of shallow furrows. Secondly, the grains in the surface layer of brass were refined, and the length of LABs (Laser Affected Zone) increased as a result of LSP. Consequently, the thickness of the worn layer for the brass with LSP was observed to be less than that of the brass without LSP.

(ii) Deformation mechanism in brass with LSP: In contrast to brass without LSP, deformation twinning was identified as the primary deformation mechanism in the worn layer of brass with LSP. The presence of mechanical twins (MTs), induced by LSP treatment, played a critical role in enhancing the tribological behavior of brass. During sliding, the MTs were able to overcome the original grain boundaries, leading to the formation of secondary twins at the MTs intersection. The growth of secondary twins resulted in an increase in grain boundaries, facilitating the refinement of grains into nanograins. These nanograins significantly enhanced the yield strength of the worn layer in brass with LSP, thereby improving its deformation resistance and contributing to the observed favorable tribological behavior.

(iii) Overall tribological performance: The combination of refined grains, increased LABs, and the presence of nanograins resulted in the improved wear resistance and overall tribological performance of brass with LSP. The findings validate the beneficial effects of LSP in enhancing the mechanical properties and deformation resistance of brass.

These comprehensive conclusions shed light on the microstructural changes and deformation mechanisms of brass with and without LSP treatment, contributing to a deeper understanding of the tribological behavior of brass and providing valuable insights for the optimization of surface treatment techniques in various industrial applications.

Data Availability The data that support the findings of this study are available on request.

Declarations

Conflict of interest All authors declare that: (i) All support funding have been marked in the manuscript; and (ii) there are no other relationships or activities that could appear to have influenced the submitted work.

References

1. Ye, C., Suslov, S., Lin, D., Liao, Y., Fei, X., Cheng, G.J.: Microstructure and mechanical properties of copper subjected to cryogenic laser shock peening. J. Appl. Phys. **110**, 083504 (2011)
2. Zhu, J.X., Li, X., Zhou, Q.H., Aghababaei, R.: On the anisotropic scratching behavior of single crystalline copper at nanoscale. Tribol. Int. **175**, 107794 (2022)
3. Zhang, D.W., Yang, G.C., Zheng, Z.B., Zhao, S.D.: Effect of forming conditions on frictional characteristic in cold bulk forming process of copper alloy. Tribol. Int. **155**, 106786 (2021)
4. Anand, D., Shrivastava, A., Ravi Kumar, D.: Size effect on surface roughness of very thin brass sheets in biaxial stretching. Mater. Today: Proc. **18**, 2448–2453 (2019)
5. Mousavi, S.E., Naghshekesh, N., Ahmadi, F., Sadeghi, B., Cavaliere, P.: Effect of lead on the crack propagation and the mechanical properties of Brass processed by ECAP at different temperatures. Mater. Sci. Eng., A **728**, 231–238 (2018)
6. Liu, L., Chi, R., Wang, J.: Effect of microstructure evolution on high cycle fatigue behavior of brass. Mater. Sci. Eng., A **732**, 326–332 (2018)
7. Mapelli, C., Mombelli, D., Barella, S., Gruttadauria, A.: Influence of the residual stresses induced by tool wear on the failure of brass electro-valves. Eng. Fail. Anal. **27**, 141–149 (2013)
8. Bushlya, V., Johansson, D., Lenrick, F., Ståhl, J.-E., Schultheiss, F.: Wear mechanisms of uncoated and coated cemented carbide tools in machining lead-free silicon brass. Wear **376–377**, 143–151 (2017)
9. Zhu, H., Zuo, X., Zhou, Y.: Recurrence evolvement of brass surface profile in lubricated wear process. Wear **352–353**, 9–17 (2016)
10. Gazizov, M.R., Belyakov, A.N., Holmestad, R., Gazizova, M.Y., Krasnikov, V.S., Bezborodova, P.A., Kaibyshev, R.O.:

The deformation behavior of the $\{111\}_{Al}$ plates in an Al–Cu–Mg–Ag alloy. Acta Mater. **243**, 118534 (2022)

11. Zheng, Z., Guo, Z., Liu, W., Luo, J.: Low friction of superslippery and superlubricity: a review. Friction **11**(7), 1121–1137 (2022)

12. Larionova, T., Koltsova, T., Fadin, Y., Tolochko, O.: Friction and wear of copper–carbon nanofibers compact composites prepared by chemical vapor deposition. Wear **319**(1), 118–122 (2014)

13. Yin, M., Shao, Y., Kang, X., Long, J., Zhang, X.: Fretting corrosion behavior of WC-10Co-4Cr coating on Inconel 690 alloy by HVOF thermal spraying. Tribol. Int. **177**, 107975 (2023)

14. Siddaiah, A., Mao, B., Liao, Y., Menezes, P.L.: Surface characterization and tribological performance of laser shock peened steel surfaces. Surf. Coat. Technol. **351**, 188–197 (2018)

15. Maleki, E., Unal, O., Guagliano, M., Bagherifard, S.: The effects of shot peening, laser shock peening and ultrasonic nanocrystal surface modification on the fatigue strength of Inconel 718. Mater. Sci. Eng.: A **810**, 141029 (2021)

16. Kishore, A., John, M., Ralls, A.M., Jose, S.A., Kuruveri, U.B., Menezes, P.L.: Ultrasonic nanocrystal surface modification: processes, characterization, properties, and applications. Nanomaterials (Basel) **12**(9), 1415 (2022)

17. John, M., Ralls, A.M., Kuruveri, U.B., Menezes, P.L.: Tribological corrosion, and microstructural features of laser-shock-peened steels. Metals **13**(2), 397 (2023)

18. Luo, K.Y., Wang, C.Y., Li, Y.M., Luo, M., Huang, S., Hua, X.J., Lu, J.Z.: Effects of laser shock peening and groove spacing on the wear behavior of non-smooth surface fabricated by laser surface texturing. Appl. Surf. Sci. **313**, 600–606 (2014)

19. Ge, M.-Z., Xiang, J.-Y., Tang, Y., Ye, X., Fan, Z., Lu, Y.L., Zhang, X.H.: Wear behavior of Mg-3Al-1Zn alloy subjected to laser shock peening. Surf. Coat. Technol. **337**, 501–509 (2018)

20. Ye, Y., Zhang, Y., Huang, T., Zou, S., Dong, Y., Ding, H., Vasudevan, V.K., Ye, C.: A critical review of laser shock peening of aircraft engine components. Adv. Eng. Mater. **25**, 2201451 (2023)

21. John, M., Ralls, A.M., Dooley, S.C., Thazhathidathil, A.K.V., Perka, A.K., Kuruveri, U.B., Menezes, P.L.: Ultrasonic surface rolling process: properties, characterization, and applications. Appl. Sci. **11**(22), 10986 (2021)

22. Lu, J.Z., Deng, W.W., Luo, K.Y., Wu, L.J., Lu, H.F.: Surface EBSD analysis and strengthening mechanism of AISI304 stainless steel subjected to massive LSP treatment with different pulse energies. Mater. Charact. **125**, 99–107 (2017)

23. Zhou, L., Long, C., He, W., Tian, L., Jia, W.: Improvement of high-temperature fatigue performance in the nickel-based alloy by LSP-induced surface nanocrystallization. J. Alloy. Compd. **744**, 156–164 (2018)

24. Larson, E.A., Ren, X., Adu-Gyamfi, S., Zhang, H., Ren, Y.: Effects of scanning path gradient on the residual stress distribution and fatigue life of AA2024-T351 aluminium alloy induced by LSP. Res. Phys. **13**, 102123 (2019)

25. Lu, J.Z., Luo, K.Y., Dai, F.Z., Zhong, J.W., Xu, L.Z., Yang, C.J., Zhang, L., Wang, Q.W., Zhong, J.S., Yang, D.K., Zhang, Y.K.: Effects of multiple laser shock processing (LSP) impacts on mechanical properties and wear behaviors of AISI 8620 steel. Mater. Sci. Eng. A-Struct **536**, 57–63 (2012)

26. Chen, X., Fang, Y., Zhang, S., Kelleher, J.F., Zhou, J.: Effects of LSP on micro-structures and residual stresses in a 4mm CLAM steel weld joints. Fusion Eng. Des. **94**, 54–60 (2015)

27. Cui, C.Y., Wan, T.Y., Shu, Y.X., Meng, S., Cui, X.G., Lu, J.Z., Lu, Y.F.: Microstructure evolution and mechanical properties of aging 6061 Al alloy via laser shock processing. J. Alloy. Compd. **803**, 1112–1118 (2019)

28. Liu, W., Man, Q., Li, J., Liu, L., Zhang, W., Wang, Z., Pan, H.: Microstructural evolution and vibration fatigue properties of 7075–T651 aluminum alloy treated by nitrogen ion implantation. Vacuum **199**, 110931 (2022)

29. Wang, F., Yao, Z., Deng, Q.: Experimental study on laser shock processing of brass. J. Univ. Sci. Technol. Beijing, Mineral, Metall, Mater **14**(6), 529–532 (2007)

30. Rigney, D.A., Karthikeyan, S.: The evolution of tribomaterial during sliding: a brief introduction. Tribol. Lett. **39**(1), 3–7 (2010)

31. Argibay, N., Furnish, T.A., Boyce, B.L., Clark, B.G., Chandross, M.: Stress-dependent grain size evolution of nanocrystalline Ni-W and its impact on friction behavior. Scripta Mater. **123**, 26–29 (2016)

32. Liu, L., Yang, C., Sheng, Y.Y.: Wear model based on real-time surface roughness and its effect on lubrication regimes. Tribol. Int. **126**, 16–20 (2018)

33. Liu, L., Sheng, Y., Liu, M., Dienwiebel, M., Zhang, Z., Dastan, D.: Formation of the third bodies of steel sliding against brass under lubricated conditions. Tribol. Int. **140**, 105727 (2019)

34. Fabbro, R., Fournier, J., Ballard, P., Devaux, D., Virmont, J.: Physical study of laser-produced plasma in confined geometry. J. Appl. Phys. **68**(2), 775–784 (1990)

35. Yang, C., Hodgson, P.D., Liu, Q., Ye, L.: Geometrical effects on residual stresses in 7050–T7451 aluminum alloy rods subject to laser shock peening. J. Mater. Process. Technol. **201**(1–3), 303–309 (2008)

36. Li, K., Hu, Y., Yao, Z.: Experimental study of micro dimple fabrication based on laser shock processing. Opt. Laser Technol. **48**, 216–225 (2013)

37. Li, K., Yao, Z., Hu, Y., Gu, W.: Friction and wear performance of laser peen textured surface under starved lubrication. Tribol. Int. **77**, 97–105 (2014)

38. Mao, B., Siddaiah, A., Zhang, X., Li, B., Menezes, P.L., Liao, Y.: The influence of surface pre-twinning on the friction and wear performance of an AZ31B Mg alloy. Appl. Surf. Sci. **480**, 998–1007 (2019)

39. Lou, S., Li, Y., Zhou, L., Nie, X., He, G., Li, Y., He, W.: Surface nanocrystallization of metallic alloys with different stacking fault energy induced by laser shock processing. Mater. Des. **104**, 320–326 (2016)

40. Furukawa, M., Horita, Z., Nemoto, M., Valiev, R.Z., Langdon, T.G.: Microhardness measurements and the Hall-Petch relationship in an Al Mg alloy with submicrometer grain size. Acta Mater. **44**(11), 4619–4629 (1996)

41. Williamson, G.K., Smallman, R.E., III.: Dislocation densities in some annealed and cold-worked metals from measurements on the X-ray debye-scherrer spectrum. Phil. Mag. **1**(1), 34–46 (1956)

42. Meyers, M.A., Vöhringer, O., Lubarda, V.A.: The onset of twinning in metals: a constitutive description. Acta Mater. **49**(19), 4025–4039 (2001)

43. Kumar, N.K., Roy, B., Das, J.: Effect of twin spacing, dislocation density and crystallite size on the strength of nanostructured α-brass. J. Alloy. Compd. **618**(618), 139–145 (2015)

44. Cao, Y., Wang, Y.B., An, X.H., Liao, X.Z., Kawasaki, M., Ringer, S.P., Langdon, T.G., Zhu, Y.T.: Grain boundary formation by remnant dislocations from the de-twinning of thin nano-twins. Scripta Mater. **100**, 98–101 (2015)

45. Liu, L., Wang, J., Zhou, J.: Characterization and analysis on micro-hardness and microstructure evolution of brass subjected to laser shock peening. Opt. Laser Technol. **115**, 325–330 (2019)

46. Cao, Y., Ni, S., Liao, X., Song, M., Zhu, Y.: Structural evolutions of metallic materials processed by severe plastic deformation. Mater. Sci. Eng. R. Rep. **133**, 1–59 (2018)

47. Mercer, C., Soboyejo, W.O.: Hall-petch relationships in gamma titanium aluminides. Scripta Mater. **35**(1), 17–22 (1996)
48. Lu, K., Hansen, N.: Structural refinement and deformation mechanisms in nanostructured metals. Scripta Mater. **60**(12), 1033–1038 (2009)